

# Three Dimensional Sheaf of Ultrasound Planes Reconstruction (SOUPR) of Ablated Volumes

Atul Ingle\*, *Student Member, IEEE*, and Tomy Varghese, *Senior Member, IEEE*

**Abstract**—This paper presents an algorithm for three dimensional reconstruction of tumor ablations using ultrasound shear wave imaging with electrode vibration elastography. Radiofrequency ultrasound data frames are acquired over imaging planes that form a subset of a sheaf of planes sharing a common axis of intersection. Shear wave velocity is estimated separately on each imaging plane using a piecewise linear function fitting technique with a fast optimization routine. An interpolation algorithm then computes velocity maps on a fine grid over a set of C-planes that are perpendicular to the axis of the sheaf. A full three dimensional rendering of the ablation can then be created from this stack of C-planes; hence the name “Sheaf Of Ultrasound Planes Reconstruction” or SOUPR. The algorithm is evaluated through numerical simulations and also using data acquired from a tissue mimicking phantom. Reconstruction quality is gauged using contrast and contrast-to-noise ratio measurements and changes in quality from using increasing number of planes in the sheaf are quantified. The highest contrast of 5 dB is seen between the stiffest and softest regions of the phantom. Under certain idealizing assumptions on the true shape of the ablation, good reconstruction quality while maintaining fast processing rate can be obtained with as few as 6 imaging planes suggesting that the method is suited for parsimonious data acquisitions with very few sparsely chosen imaging planes.

**Index Terms**—ablation, shear stiffness, sheaf, 3D reconstruction, ultrasound, shear wave elastography, electrode vibration

## I. INTRODUCTION

**L**IVER cancer is one of the most common forms of cancer in the world with a very high mortality index (mortality to incidence ratio of 93% (2008)) making it

Atul Ingle is with the Departments of Electrical and Computer Engineering and Medical Physics, University of Wisconsin–Madison, Madison, WI 53706 USA. Corresponding author email: [ingle@wisc.edu](mailto:ingle@wisc.edu), phone: 408-823-7537.

Tomy Varghese is with the Departments of Medical Physics and Electrical and Computer Engineering, University of Wisconsin–Madison, Madison, WI, 53706 USA. Email: [tvarghese@wisc.edu](mailto:tvarghese@wisc.edu).

Original manuscript received November 21, 2013. Revised March 11, 2014. Accepted April 23, 2014.

This work was supported in part by NIH-NCI grants R01CA112192-S103 and R01CA112192-06.

one of the leading cause of cancer related deaths [1]. Tumor ablation therapy is a minimally invasive procedure that can be used to treat smaller localized tumors. Radiofrequency (RF) and microwave ablation procedures involve insertion of an ablation needle into the affected area and inducing localized heating to thermally coagulate the cancerous cells. Accurate real-time visualization of the ablated region has clinical value because it can provide immediate feedback to the clinician about the extent of ablation. Accurate control of the ablation volume is crucial for preventing recurrence of tumors, arising from the presence of untreated cancerous cells.

The problem of boundary delineation for tumor visualization has been an important signal processing issue in various medical imaging modalities. Since liver tumors may not have sufficient echogenic contrast *vis-à-vis* healthy liver tissue [2], [3], [4], visualizing them on a conventional B-mode image is challenging. Ultrasound elastography attempts to derive local mechanical properties of tissue from estimated displacements [5]. It has potential to augment traditional B-scans and assist the clinician in delineating ablation boundaries more accurately. Unlike X-ray computed tomography (CT) or magnetic resonance imaging (MRI), traditional ultrasound elastography has been limited to single imaging planes, over which strain is estimated, and the Young’s modulus (stiffness) is reconstructed by solving the inverse problem [6], [7], [8], [9]. Shear wave velocity (SWV) and shear modulus can also be estimated for these imaging planes [10]. The accuracy of such methods is limited by the underlying assumptions about tissue elasticity and other geometric and boundary effects.

Two dimensional (2D) ultrasound has been widely applied to tissue stiffness measurements in ablation monitoring procedures in the liver [11], [12], [13], [14]. The ablation needle appears hyperechoic in a traditional B-mode scan, and hence provides a way to guide the needle placement in the tumor and for aligning the image plane when monitoring ablations. Multiple frames of ultrasound echo data acquired after ablation can be used for both quasistatic and dynamic ultrasound elastography to reveal stiffness variations in the imaged plane. Quasistatic imaging [6], [15] can be performed by manually

perturbing the medium using the ablation needle and displaying the rate of change of displacements with depth (strain). Prior information about the shape of the ablated area can be harnessed to improve boundary visibility in the strain image [16]. Alternatively, dynamic elastography methods can also be used to visualize tissue mechanical properties. Acoustic radiation force imaging (ARFI) [17], [18] involves application of high frequency focussed ultrasound pulses to create localized displacement in liver tissue. These displacements can be tracked using radiofrequency ultrasound echoes and generate an ARFI image. By rapidly moving the focal point of the ARFI pulses, supersonic shear imaging (SSI) modality produces a “Mach cone” shear wavefront [19] which is tracked as a function of time to infer stiffness moduli [20]. Another approach aims at mapping viscoelastic properties of ablated versus healthy liver by imaging shear waves over a range of frequencies [21], the hypothesis being that ablation causes changes in (frequency dependent) dispersive properties of liver tissue. In the present paper, the frequency dependent variation of SWV is ignored by estimating only the group velocity by tracking a shear wave pulse (which is essentially broadband in the frequency domain).

In this paper, 2D electrode vibration shear wave imaging method is extended to three dimensions (3D) by utilizing radiofrequency echo signals acquired over a “sheaf” of imaging planes. A sheaf is defined as a collection of planes that intersect along a common axis. The 3D reconstruction algorithm is termed “**Sheaf Of Ultrasound Planes Reconstruction**” or **SOUPR**. This cylindrically symmetric method of acquisition is naturally suited to electrode vibration elastography (EVE) where shear wavefronts travel outward from a vibrating needle which acts as a line source of shear waves [7]. Moreover, the overall shape of the ablation is approximately cylindrically symmetric with the ablation needle as the axis of symmetry.

There has been growing interest in 3D ultrasound imaging and elastography; one evidence being the evolution of literature on this topic in the last two decades. Elliott [22] notes the increasing use of 3D data acquisition among ultrasound sonographers to circumvent the limitations of traditional 2D ultrasound. Various authors have analyzed reconstruction algorithms for 3D B-mode imaging [23], [24] of different anatomical structures using a variety of transducer types and scanning arrangements. Quasistatic freehand elastography has received much research attention [25], [26]. These 2D elastography techniques can be naturally extended to 3D in various ways. Freehand elastography can be performed by manually translating the transducer probe through

parallel imaging planes. Alternatively, a “wobbler” that mechanically rotates or translates an array transducer using a stepper motor may be used. Other authors have proposed using more elaborate robotic techniques [27] for accurate control of the location of the transducer in 3D space. Each image plane is processed using standard elastography algorithms and a 3D rendering is generated [28]. Freehand elastography can be augmented with accurate optical [29] or magnetic position sensors that precisely record the coordinates of the transducer. Fortunately, for tumor ablation monitoring using EVE, the ablation needle provides a good reference for manually aligning the imaging plane. Elaborate tracking and registration systems have the potential to improve reconstruction accuracy. The present work uses only a crude alignment strategy relying on the assumptions that the underlying 3D structure is fairly symmetric about the needle axis, independent sheaves (with relatively small misregistration errors) are acquired, and the final 3D reconstructions are averaged.

Results on 3D quasistatic strain [28], [30] and transient SWV reconstruction [31] for prostate imaging have been reported in literature. Lee *et al.* [32] have reported significant improvement in detection of cancerous breast lesions when B-mode imaging is augmented with freehand 3D shear wave imaging. Literature on full 3D reconstruction of SWVs and shear stiffness is still in its nascency. In recent work by Wang *et al.* [33], 3D reconstruction of muscle fiber orientation was achieved by mapping group and phase velocities of the shear wave set up using acoustic radiation force. Although the use of matrix transducer arrays for volume ultrasound imaging is gathering pace, linear and curvilinear array transducers are still the most widely used transducer types. Therefore, the ability to generate volume rendering akin to CT or MRI using 2D ultrasound data has clinical value [22].

## II. MATERIALS AND METHODS

### A. Electrode Vibration Setup

A schematic view of an EVE setup is shown in Fig. 1. The needle mimics an RF electrode or a microwave antenna that is used in an ablation procedure. This needle is firmly bound to a stiff ellipsoidal inclusion which mimics ablated tissue. This ellipsoid is embedded in a softer background material that mimics healthy (cancer-free) tissue. Additionally, an irregularly shaped intermediate stiffness region is present on one side of the ellipsoid that simulates partially ablated tissue. A pulse deformation is applied to the needle using an external actuator (Physik Instrumente, Germany) which

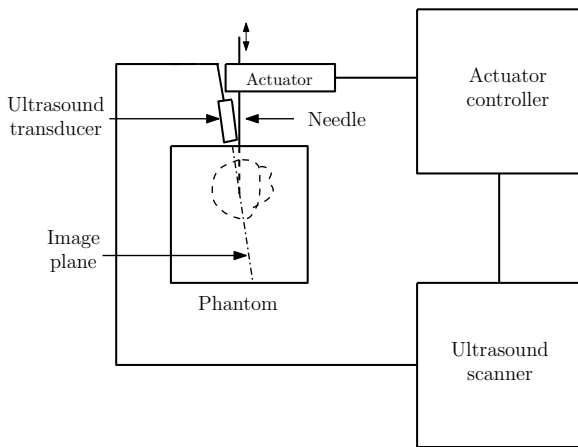


Fig. 1. This schematic shows the data acquisition system used in electrode vibration elastography experiments. The needle is vibrated using an actuator. Data acquisitions are phase-locked by synchronizing the ultrasound scanner pulse sequencing with the actuator motion. The image plane is adjusted in such a way that it contains the needle.

is attached to the needle. This sets up a shear wave pulse where the wave source is a line coinciding with the needle and the shear wavefronts travel cylindrically outward and away from this line.

Since the frame rates with traditional B-mode ultrasound imaging are not sufficient to track a shear wave pulse (which travels with a velocity of a few meters per second), a sequential tracking technique developed by DeWall and Varghese [8] was used. This is similar to the phase locking technique used in MRI elastography [34]. In this method, the needle is vibrated multiple times and with each vibration a different location at a specified lateral distance away from the needle is scanned using the ultrasound system (Ultrasonix SonixTouch, Richmond, BC, Canada). Vertical strips of radiofrequency ultrasound echo data are then registered and assembled to obtain “pseudo-high-frame-rate” data over the entire image plane as a function of time. The phase-locked acquisition scheme assumes that the needle is vibrated identically in each cycle and the image plane is not changed during the acquisition. Alternatively, high frame rate plane wave ultrasound imaging [35] can be used to scan the entire image plane in a single transmit. In case of periodic tissue motion with only a few constituent frequencies, the method of radiofrequency phasor alignment described in the paper by Baghani *et al.* [36] may be applied.

In order to reconstruct a 3D SWV map, data is acquired over a subset of a sheaf of planes. This subset can be chosen in such a way that the planes are equispaced in angle. For example, a sheaf of four imaging planes is shown in Fig. 2. Although equispaced planes were used in the present study, the SOUPR algorithm

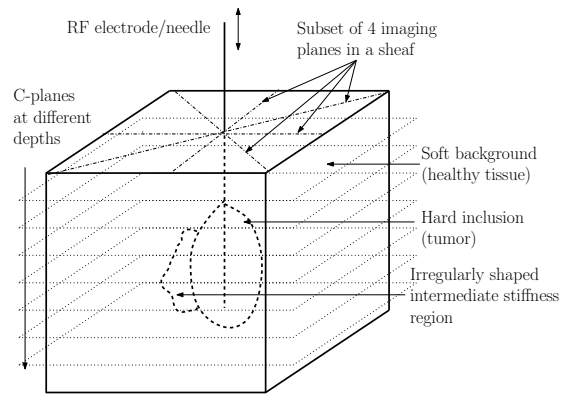


Fig. 2. The tissue-mimicking phantom used in this study consisted of a hard inclusion embedded in soft background and an irregularly shaped partially ablated region on one side. A subset of a sheaf of imaging planes containing four equiangular planes passing through a line that coincides with the ablation needle is shown. A stack of C-planes over which the shear wave velocities are interpolated is also shown. The needle was vibrated vertically to set up a shear wave pulse.

presented here can also handle scattered data points from irregularly spaced imaging planes. The transducer was manually adjusted to image specific angular locations in the sheaf. Guide markers on the phantom container walls were used to align the angle of the imaging plane. The number of planes was varied from 4 to 16 to study the effect on reconstruction quality with increasing number of planes. Each volume reconstruction was repeated using five independent datasets to ensure that slight discrepancies in the locations of individual image planes are averaged out. This method relies on misregistration errors being small enough to be considered as part of the additive measurement noise. In general, the method may fail if there is significant relative translation or rotation between two volumes. If greater accuracy in transducer placement is desired, feedback control systems like one described by Abolmaesumi *et al.* [37] may be employed. Such systems are beyond the scope of the present work.

### B. Tissue Mimicking Phantom

The tissue-mimicking (TM) phantom based study involved data acquisition from a TM phantom constructed using an oil-in-gelatin dispersion. This dispersion is composed of microscopic oil droplets dispersed in a gelatinous matrix. The proportion of oil in the matrix controls the local stiffness. The density of this TM material is very close to that of water ( $1000 \text{ kg/m}^3$ ). Further discussion on the manufacturing process and properties of the TM phantom material can be found in the paper by Madsen *et al.* [38]. The phantom used in this study consists of a stiff ellipsoid embedded in a softer background. This arrangement is designed

to mimic the presence of a partially ablated tumor in cirrhotic liver tissue. Additionally, a small irregularly spaced area of slightly lower stiffness than the ellipsoid is present on one side of the inclusion. This mimics the presence of partially ablated cancerous tissue.

A stainless steel rod was glued to the center of the ellipsoid in order to mimic the role of the ablation needle in an actual ablation procedure. This rod was used for generating shear waves in the phantom with the help of an actuator. A 3D schematic of the phantom is shown in Fig. 2. The TM phantom gelatin block is  $14\text{ cm} \times 14\text{ cm} \times 9\text{ cm}$ . This block is placed in an open top 1 cm thick acrylic container. A 2 cm deep layer of safflower oil poured on the top surface of the TM phantom prevents desiccation.

### C. Algorithm

The 3D reconstruction algorithm SOUPR consists of four distinct data processing steps, starting with the acquisition of beamformed radiofrequency ultrasound echo data, finally leading to the 3D stack of C-planes of SWV estimates:

- 1) Displacement estimation from beamformed echo data over each imaging plane.
- 2) Wavefront localization to obtain time to peak (TTP) [39] displacement at different locations in the imaging plane.
- 3) SWV estimation from TTP plots to obtain SWV maps over each imaging plane.
- 4) Smooth function approximation on a grid over each C-plane.

As seen in Fig. 2, each C-plane is perpendicular to all the imaging planes. The SOUPR algorithm presented here effectively breaks down a 3D reconstruction problem into a sequence of decoupled 2D function approximation problems. Each C-plane is processed separately and the final 3D reconstruction is generated by stacking them together.

The four steps are discussed in the following subsections.

1) *Displacement Estimation*: Ultrasound echo data is acquired over each imaging plane as described previously in Section II-A. The sequential tracking acquisition enables axial strips to be assembled into individual frames to obtain high frame rates for tracking shear waves. These frames provide snapshots of the underlying medium at different time instants. Frame-to-frame displacements are estimated using a standard 1D cross-correlation algorithm [40]. An axial displacement estimation routine is used with a window length of 2 mm and 75% overlap. This procedure is repeated over the

entire imaging plane to obtain a displacement vs. time profile at each pixel [41].

2) *Wavefront Localization*: The high frame rate displacement data is used to localize the shear wave pulse. It is assumed that the wave travels purely laterally away from the needle. The time of arrival of the wave at different locations away from the needle is recorded by finding the time of peak displacement [39], [42]. A frequency domain filter discards any frequency components that are smaller than 10% of the largest component of the frequency spectrum of the displacement vs. time profiles. This filters out any “high frequency” noise components in the displacement-time profiles making it easier to locate the peak. A quadratic fit with a 5-point window is used around the peak to get sub-frame-number resolution for the location of the peak.

3) *Imaging Plane Reconstruction*: The TTP data obtained over each image plane can be used to estimate SWV by calculating the reciprocal of the slope of the TTP curves at different depths. However, some form of smoothing must be applied prior to calculating the slope because differentiating noisy data will amplify noise. An important consideration for this noise filtering algorithm is to preserve edge details between the stiff inclusion and the soft background. An optimization algorithm that fits a continuous piecewise linear function to the noisy TTP curves [43] is designed with a function model parametrized by the locations of breakpoints and slopes of individual segments. Let the number of segments in the fit be denoted by  $B$ , the unknown breakpoint locations by  $\{\lambda_i\}_{i=0}^B$  and unknown segment slopes by  $\{m_i\}_{i=1}^B$ . A piecewise linear function is modeled as:

$$f(x) = \sum_{i=0}^{B-1} \chi_{[\lambda_i, \lambda_{i+1})}(x) \left[ m_{i+1}(x - \lambda_i) + \sum_{j=1}^i m_j(\lambda_j - \lambda_{j-1}) \right] \quad (1)$$

where the “indicator function”  $\chi_A(t) = 1$  when  $t \in A$  and zero otherwise. A specific case of this function model with  $B = 3$  is shown in Fig. 3. It is assumed that the noisy TTP data,  $\{y_i\}_{i=1}^N$ , originates from this true underlying function. Therefore a constrained least-squares problem can be formulated to estimate the free parameters in this model:

$$\begin{aligned} & \text{minimize} && \frac{1}{N} \sum_{i=1}^N (y_i - f(x_i))^2 \\ & \text{subject to} && m_i > 0, \text{ and } \lambda_0 < \lambda_1 < \dots < \lambda_B. \end{aligned}$$

The least-squares optimization problem is solved using a standard sequential quadratic programming [44]

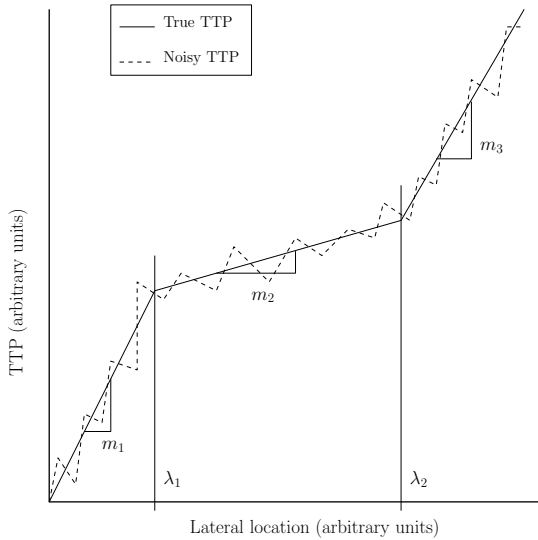


Fig. 3. A piecewise linear model with unknown breakpoints ( $\lambda_1, \lambda_2$ ) is used for estimating local slope values ( $m_1, m_2, m_3$ ). The reciprocals of these slope values are used as estimates of local shear wave velocities at different lateral locations away from the electrode.

numerical optimization routine. Other methods such as interior point optimization, log-barrier algorithms, or stochastic optimization methods such as simulated annealing [45] can also be used.

In reality, the number of segments  $B$  is not known *a priori*. Therefore the algorithm must choose a reasonable  $B$  automatically. This problem of “model order selection” is handled using the Akaike information criterion (AIC) [46] which trades off mean-squared error and model complexity by minimizing the following function by choice of  $B$ :

$$\text{AIC} = N \log(\text{MSE}/N) + (2B - 1)$$

where MSE is the residual mean squared error between the data and the fit. The intuition behind using this criterion is that it not only penalizes a bad fit (large MSE) but also penalizes the number of segments (model complexity), thereby providing a safeguard from overfitting. The optimization problem is solved with  $1 \leq B \leq 10$  and the best  $B$  is chosen to minimize AIC. Finally the SWV map for every image plane is filtered using a  $4 \text{ mm} \times 2 \text{ mm}$  median filter to remove any outliers.

The image plane containing the partially ablated region is also imaged using a commercial Supersonic Imagine (Aix-en-Provence, France) scanner using the ShearWave™ Elastography mode. SWV estimates are obtained using ROIs placed in the three different regions of the phantom.

4) *C-plane Function Approximation*: SWV estimates on each C-plane are obtained from a second function approximation routine. Fig. 2 also illustrates a set of C-

planes over which the SWV values are interpolated. The goal is to provide smooth reconstructions of SWV values using a fine grid on every C-plane.

Depending on the number of planes imaged in the sheaf, SWV estimates are available along many concurrent radial lines passing through the needle axis on each C-plane. (However, it is worth noting that this step of the SOUPR algorithm is quite general and can be applied even if data is not acquired in a sheaf pattern.) For convenience, let  $\mathbf{x}$  denote a vector of the unknown values of SWVs on the user defined C-plane grid and let  $\mathbf{b}$  denote the vectorized version of the known SWV values (data) along radial lines on the same C-plane. In general, the known data points do not coincide with grid points. Since this is now a 2D smoothing problem on a particular C-plane, a local bilinear interpolation scheme is used. Each known function value is expressed as a linear combination of the four neighboring grid points. The weighting coefficients for the grid neighbors of each data point are represented using rows of a matrix  $\mathbf{A}$ . The number of rows in  $\mathbf{A}$  is equal to the length of  $\mathbf{b}$  and the number of columns is equal to the length of  $\mathbf{x}$ . In theory, the unknown function values on the grid can be computed by solving the system of linear equations  $\mathbf{A}\mathbf{x} = \mathbf{b}$ .

Note that the number of unknowns (grid locations) in the problem can be much larger than the number of points at which the stiffness estimates are actually known. So  $\mathbf{A}$  may not be full rank (it has fewer rows than columns) which makes the system of linear equations ill-posed. This ill-posedness is circumvented by adding an extra term which penalizes a large value of the derivative at any point in the reconstruction. Since differentiation in the case of discrete data is simply a finite difference operation, it can be compactly represented using another (square) matrix  $\mathbf{B}$ . Second order central differences (Laplacian) are used here to penalize the second derivative of the underlying function. The derivative at each grid node can be expressed as a linear combination of its four neighboring grid nodes. The following least-squares optimization problem can be used to solve for the unknown values on the grid:

$$\underset{\mathbf{x}}{\text{minimize}} \|\mathbf{A}\mathbf{x} - \mathbf{b}\|^2 + \eta \|\mathbf{B}\mathbf{x}\|^2 \quad (2)$$

where  $\eta > 0$  is a regularization parameter that controls the amount of smoothing. Fortunately, this problem has a closed form solution given by:

$$\mathbf{x} = (\mathbf{A}^T \mathbf{A} + \eta \mathbf{B}^T \mathbf{B})^{-1} \mathbf{A}^T \mathbf{b}. \quad (3)$$

The aforementioned problem setup is closely related to the idea of “Tikhonov regularization” for ill-posed problems [47, Ch. 8]. Explicit computation of the matrix

inverse in (3) should be avoided in practice. For the present setup, each row of  $\mathbf{A}$  and  $\mathbf{B}$  contain at most four and five non-zero entries respectively, and the matrix in the parentheses in (3) is sparse, symmetric and block diagonal which can be efficiently inverted using sparse factorization algorithms [44]. This also bypasses any computational issues with large matrix dimensions thereby allowing use of fine reconstruction grids.

If the smoothing parameter  $\eta$  is chosen arbitrarily, larger values will force the final fit to be closer to the null space of the penalty function which induces smoothness, whereas small values will result in a more undulating fit. However an objective method for selecting this parameter is necessary for studying reconstruction quality using summary statistics like the mean and standard deviation calculated from regions of interest in the reconstructed image. For this study, an automatic method called leave-one-out ordinary cross-validation (OCV) is used to circumvent any user induced variability from different values of  $\eta$ . In this method, the fitting routine is repeatedly run by excluding one data point at a time and calculating the OCV score function given by:

$$\text{OCV}(\eta) = \frac{1}{M} \sum_{k=1}^M (\hat{b}_k - b_k)^2$$

where  $M$  denotes the number of data points,  $b_k$  denotes the *known* data value at a skipped data point location  $k$ , and  $\hat{b}_k$  denotes the value *predicted* by the optimization procedure when all but the  $k^{\text{th}}$  data point are used to solve (2). A grid search is then used to arrive at the choice of  $\eta$  that minimizes this score function. The smoothing parameter chosen in this manner also has a desirable statistical property of minimizing the cross-validation score which is an unbiased estimator of the mean squared error risk [48, Sec 5.3]. Example C-plane reconstructions with three different values of  $\eta$  are shown in Fig. 4. These plots were generated using a test function of two dimensions:  $f(x, y) = 1$  when  $x^2 + y^2 \leq 1$  (unit circle centered at the origin), and zero otherwise, with the domain  $-2 \leq x, y \leq 2$ . Gaussian noise was added to this function to simulate measurement errors in the shear wave velocity and registration errors due to misalignment of the image plane angle. The function values were then imputed on a grid using (3). The “correct” value of  $\eta$  for this case was found by minimizing  $\text{OCV}(\eta)$  shown in Fig. 5. In the interest of processing time,  $\eta$  was estimated only once per dataset using the C-plane at half the maximum depth. It can be re-estimated for every C-plane if desired.

In order to better understand the effect of noise and varying number of image planes on the reconstruction

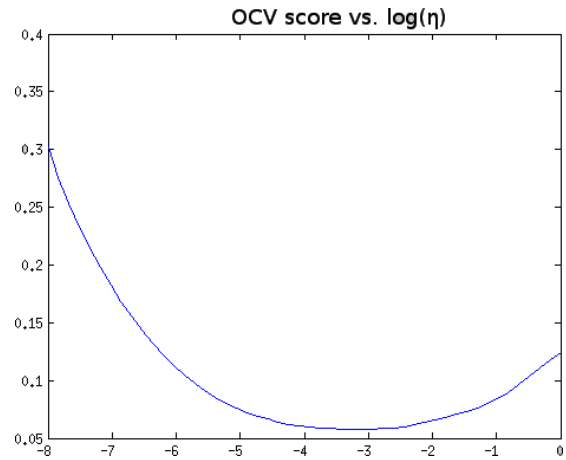


Fig. 5. OCV plot vs  $\log(\eta)$ . The minimizer in this case is approximately  $\eta = e^{-3}$ .

quality of this algorithm, a Monte Carlo simulation experiment was performed using a single C-plane. Using the same test function as above, synthetic data is generated with 4, 6, 12 and 16 concurrent radial lines with 80 equidistant samples along each line. Gaussian noise for different signal to noise ratios (SNR) was added to simulate measurement errors. Since the maximum test function value is 1, SNR is defined as  $20 \log_{10}(1/s)$  where  $s$  is the standard deviation of simulated Gaussian noise. This noisy data was processed with the SOUPR algorithm to reconstruct C-plane function values  $\hat{f}(x, y)$  on a  $100 \times 100$  grid in the domain  $-2 \leq x, y \leq 2$ . Reconstruction mean squared error was calculated using  $\frac{1}{10^4} \sum_{i=1}^{100} \sum_{j=1}^{100} \left| f\left(\frac{4i-202}{99}, \frac{4j-202}{99}\right) - \hat{f}\left(\frac{4i-202}{99}, \frac{4j-202}{99}\right) \right|^2$ , where the scaling and shifts ensure that the functions  $f$  and  $\hat{f}$  are evaluated in the domain  $-2 \leq x, y \leq 2$ . This simulation was repeated 10,000 times. Results are shown in Section III-A.

#### D. Data Analysis

The quality of 3D reconstructions was gauged by calculating the contrast (C) and contrast-to-noise ratio (CNR) for pairs of regions in the TM phantom. In conventional 2D elastography, these statistics are calculated over carefully chosen regions of interest (ROI). For the 3D case, the same idea is extended here by choosing parallelepiped shaped ROIs, with lateral and elevation dimensions of 5 mm each and 10 mm axially. These statistics are presented in decibel units using the following formulas [40], [49]:

$$C = 20 \log_{10} \left( \frac{\mu_1}{\mu_2} \right)$$

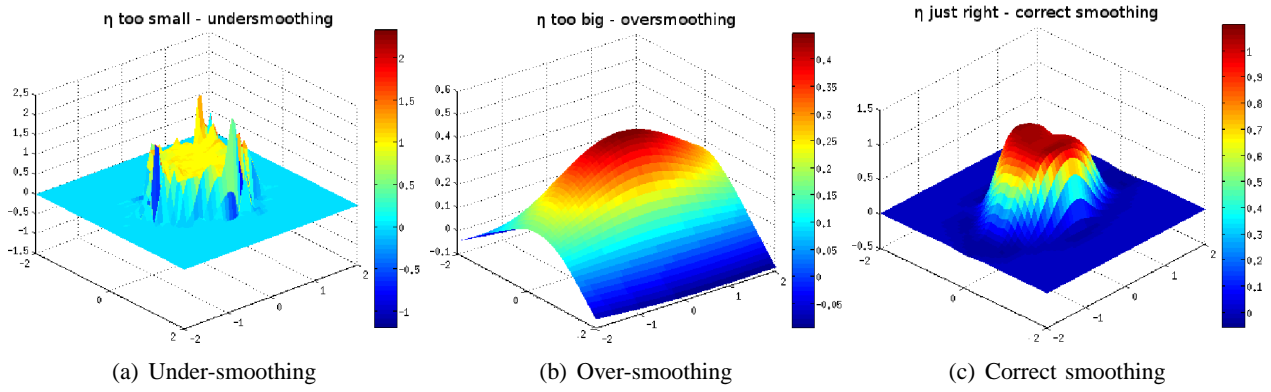


Fig. 4. This figure shows the effect of using different values of the smoothing parameter  $\eta$  in the fitting procedure applied to simulated noisy data. When  $\eta$  is too small, the resulting fit follows the noise as seen in (a), whereas if  $\eta$  is too big it causes over-smoothing as seen in (b). The correct smoothing parameter value strikes an “optimal” balance as seen in (c). This value is chosen to minimize the OCV score plotted in Fig. 5.

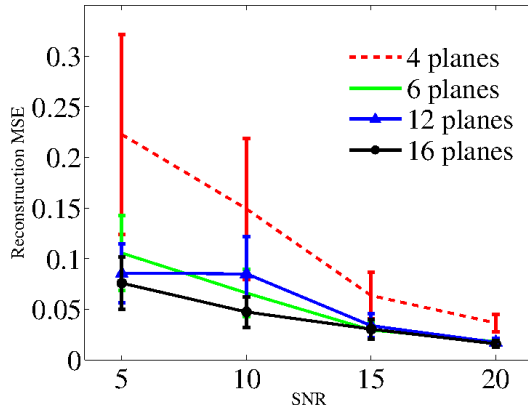


Fig. 6. Mean squared reconstruction error (MSE) from simulated data at different noise levels and varying number of image planes. The reconstruction error is largest when only 4 image planes are used. No significant improvement is obtained by increasing the number of planes from 6 to 16, as seen from the overlapping errorbars around the MSE values.

and

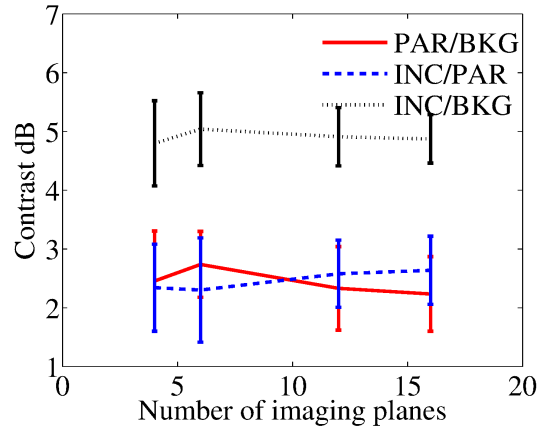
$$\text{CNR} = 20 \log_{10} \left( \frac{2(\mu_1 - \mu_2)^2}{\sigma_1^2 + \sigma_2^2} \right).$$

where  $\mu$  and  $\sigma$  respectively denote the mean and the standard deviation values of the SWVs calculated over each ROI and the subscripts indicate two distinct media. The mean and standard deviations over 5 independent datasets were obtained after converting to dB.

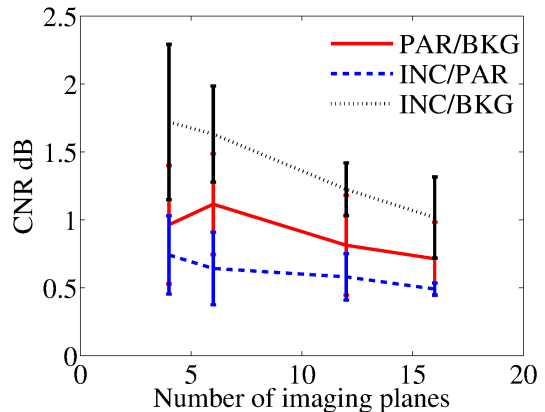
### III. RESULTS

#### A. Simulations

Results of Monte Carlo simulations are shown in Fig. 6. Note that the reconstruction error decreases with increasing SNR, irrespective of the number of image planes used. In all cases the reconstruction error was



(a) Contrast



(b) CNR

Fig. 9. Plots of (a) Contrast and (b) CNR as a function of the number of imaging planes. Contrast and CNR plots are for three different pairs of regions. (BKG=background, PAR=partially ablated, INC=inclusion)

TABLE I  
SHEAR WAVE VELOCITY ESTIMATES

# imaging planes	background	partially ablated	inclusion
4	$0.7642 \pm 0.0722$	$1.0106 \pm 0.0218$	$1.3264 \pm 0.1039$
6	$0.7454 \pm 0.0432$	$1.0205 \pm 0.0195$	$1.3357 \pm 0.1395$
12	$0.7623 \pm 0.0612$	$0.9947 \pm 0.0251$	$1.3412 \pm 0.1007$
16	$0.7608 \pm 0.0673$	$0.9814 \pm 0.0256$	$1.3324 \pm 0.1019$
SSI	$0.9 \pm 0.07$	$1.1 \pm 0.05$	$1.2 \pm 0.03$

Values of SWV (in m/s) for the three regions of interest are shown. The number of imaging planes used for 3D reconstruction is varied from 4 to 16. The mean and standard deviations were calculated over 3D parallelepiped shaped ROIs. For comparison, measurements from the commercial Supersonic Imagine (SSI) ShearWave™ Elastography imaging mode are also shown. Note that the SSI measurements were obtained using conventional 2D ROIs from only a single imaging plane with the partially ablated region in view (cf. Fig. 12).

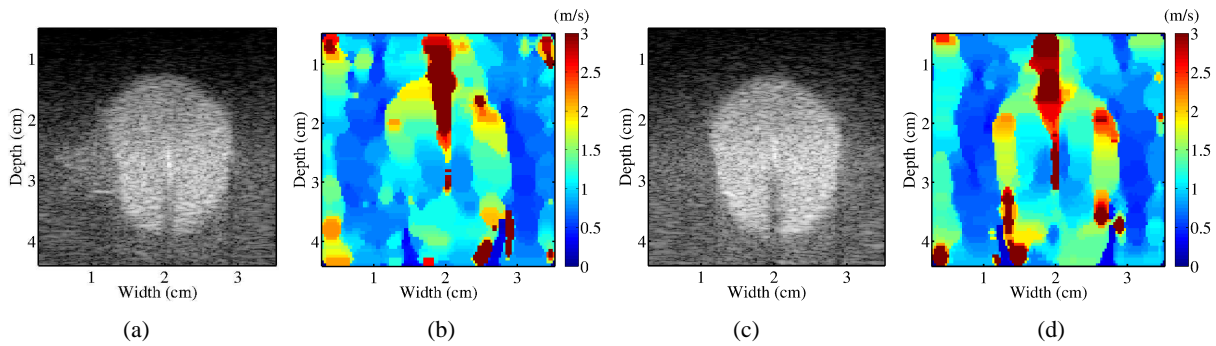


Fig. 7. Ultrasound B-mode image and respective shear wave velocity (SWV) images are shown. Note the clear visualization of the partially ablated region seen on B-mode in (a) and in the shear wave image obtained using the piecewise linear fitting algorithm in (b). B-mode (c) and SWV reconstruction (d) for an image plane not including the partially ablated region are also shown for comparison. Backscattered intensity was varied in the phantom to visualize normal, ablated and partially ablated areas in the B-mode reference images.

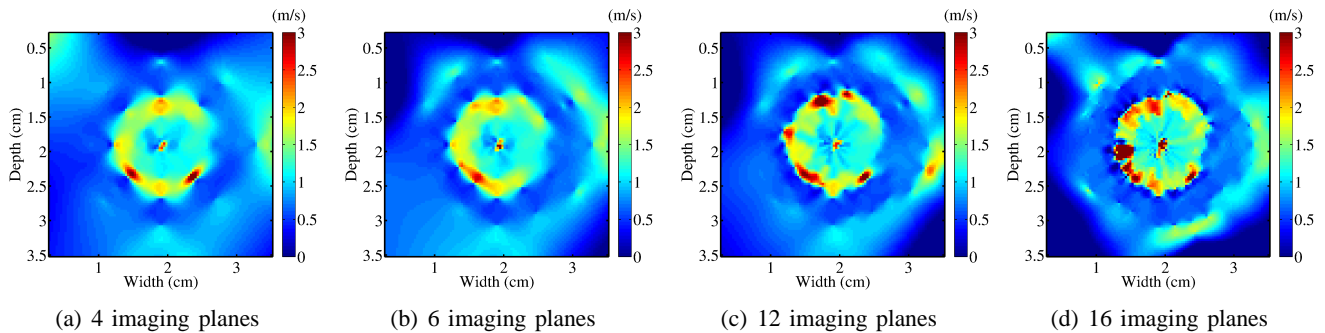


Fig. 8. Example C-plane reconstructions of shear wave velocity at an axial depth of 2.8 cm with different number of imaging planes. Observe that as more planes of data are introduced, the variability and finer detail in the boundary increases, and the “wheel spoke” artifact becomes less pronounced.

largest when 4 image planes are used. On average, the 16 plane case gives the best reconstruction accuracy, but the error bars overlap considerably when the number of planes is 6, 12 or 16. This suggests that for the ideal case of a perfectly radially symmetric inclusion, increasing the number of image planes beyond 6 does not lead to any significant improvement in reconstruction quality.

### B. Phantom Data

The reconstructed SWV maps for two of the imaging planes over which radiofrequency ultrasound data loops were acquired are shown in Fig. 7. SWV reconstructions were performed by applying piecewise linear fitting to the raw TTP data as illustrated in Fig. 3. The first image plane passes through the partially ablated region which

can be visualized in both the B-mode and the SWV reconstruction while the second plane is aligned such that the partially ablated region is not seen. Note that these regions of varying stiffness are not as easily visible in real tissue using a B-mode scan. But they can be easily seen here because the TM phantom material was designed to have different acoustic echogenicities for different regions. C-plane slices using different numbers of angular planes between 4 and 16 are shown in Fig. 8. The partially ablated region can be seen on the right side of the inclusion in all the four C-planes.

The estimated SWVs shown in Table I do not change significantly as the number of planes in the sheaf was changed. This is because the structure of the phantom is quite symmetrical, so on average the measured SWVs do not vary when new planes of data are added. The regularized function estimation framework described here is also related to classical statistical learning theory: the choice of  $\eta$  is related to the so called bias-variance tradeoff [50, Ch. 2, Sec. 2.2.2]. A small value of  $\eta$  will produce an undulating fit, i.e., an estimator with low bias but high variance. On the other hand, larger value of  $\eta$  will reduce the variance and increase the bias. AIC in the piecewise linear fitting algorithm and regularization in the optimization problem are both ways to trade off some variance at the cost of introducing a bias in the estimated function. As a result of the smoothing, the SWV estimates shown in Table I are lower than the true values for the phantom calculated using the known material stiffness (Young's modulus). But they agree quite well with the SWV estimates obtained using SSI shown in the last row of the table. Moreover, delineation of ablated and partially ablated regions, which is of paramount importance, can be easily seen in the C-plane images.

There are several tradeoffs associated with increasing the number of imaging planes for 3D reconstruction. Additional planes would require significantly more data acquisition and processing to obtain SWV reconstructions. A quantitative evaluation of improvements obtained by increasing the number of imaging planes is therefore necessary to determine a reasonable number of planes needed for fast imaging. Image quality metrics calculated over 5 independent datasets are shown in Fig. 9. The largest contrast of about 5 dB in Fig. 9(a) is obtained when comparing the soft background with the hard inclusion, also imaged with 6 imaging planes. A highest CNR of 1.5 dB is obtained using 6 imaging planes in the sheaf as illustrated in Fig. 9(b). As one would expect, the highest contrast values were seen between the inclusion-background regions. In general, there is a decreasing trend in all image quality statistics as the number of

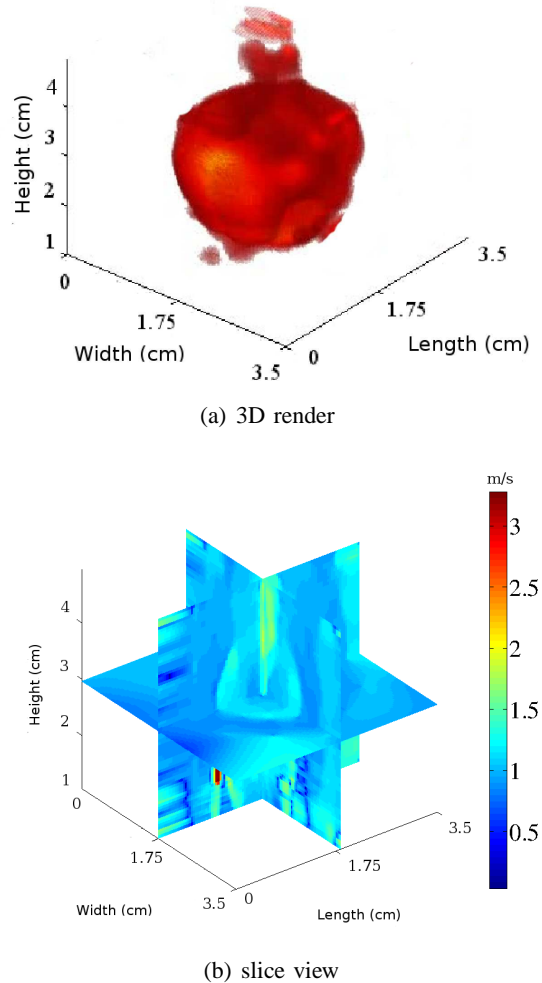


Fig. 10. (a) 3D reconstructed volume of the inclusion using 6 imaging planes obtained by thresholding. (b) Three slice view of the 3D volume with SWV shown in m/s.

planes was increased.

The full 3D reconstruction using 6 imaging planes is shown in Fig. 10. This is created by stacking together the individual C-planes. This 3D render should be interpreted with caution because only an apparent estimate of the shear wave velocities is obtained. It should not be misconstrued as a solution of a full 3D shear wave propagation inverse problem. Fig. 10(a) is obtained by thresholding and is for visualization only. Numerical information is shown in the three-slice view in Fig. 10(b).

#### IV. DISCUSSION

This paper presented a novel technique for acquiring, processing and displaying a 3D rendering of the SWV distributions for ultrasound shear wave elastography using a stack of C-plane reconstructions. The C-plane visualizations of the ablation slices can also be utilized to clearly delineate ablation boundaries. The sheaf of ultrasound planes reconstruction (SOUPR) algorithm is

presented and validated using TM phantom experiments for EVE.

A piecewise linear fit was used in this paper to accentuate change points with the goal of improving boundary delineation in the reconstructed SWV maps on individual scan planes. Other noise filtering methods such as least squares linear or polynomial fitting [51] or Kalman filtering [52] can also be used. The idea of Tikhonov regularization for smooth function approximation was previously applied to displacement estimation by Rivaz *et al.* [53]. In contrast, this paper uses regularized optimization to reconstruct smooth shear wave velocity maps from undersampled grids. It is worth noting that the second order finite differencing regularization term used in this work can be replaced with first or higher order derivatives or any other types of penalty functions that promote smoothness. The key requirement is the ability to express the penalty as a linear operation so that the formulation in (2) can still be used.

The contrast stays almost constant as the number of planes in the sheaf was increased. The CNR quality metric shows a decreasing trend as the number of planes is increased. This may be a side effect of the smooth C-plane fitting algorithm. The fitting algorithm approximates a smooth surface in regions where there are no data points. With fewer number of planes there are larger regions with no data points, resulting in a visually smoother fit which corresponds to better CNR in the image. On the other hand, when the number of image planes is increased, the voids are much smaller. Therefore the first term in the optimization problem (2) exerts greater influence forcing the surface fit to appear more undulating. To enable fairer comparison between reconstructions performed with different number of image planes, these quality metrics may have to be modified by accounting for these effects.

Various artifacts can also be seen in the SWV maps and the C-plane reconstructions. These are summarized in Fig. 11. High velocity artifacts appear above and below the inclusion because the assumption of purely lateral shear wave propagation may not hold those regions. Removal of such artifacts has been studied previously [54] and can be incorporated into the 3D reconstruction algorithm. High velocity artifacts are also seen close to the edge of the image plane due to limited imaging aperture in those areas. Methods for removal of artifacts due to wavefront distortion and reflection have been discussed previously [10], [55] and have the potential to improve reconstruction quality for the 3D case too. Low velocity artifacts seen in areas adjacent to the needle have been observed in previous EVE studies [8] and require further investigation. The authors conjecture that

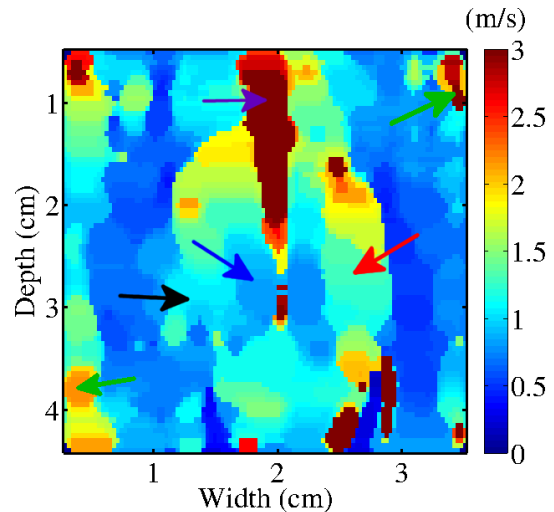


Fig. 11. This figure shows various structures and artifacts present in the SWV image plane. The red arrow points to the stiff ablated region and the black arrow points to the partially ablated region. There is a low velocity artifact near the needle shown by the blue arrow at the center. There are high velocity artifacts close to the edge of the image shown with green arrows in the top right and bottom left corners. The violet arrow near the top of the image plane points to a high velocity artifact due to the needle.

the shear wave pulse takes some time to accelerate to its maximum speed after the needle is vibrated resulting in perceived low velocity close to the needle source. This artifact may not be a serious hurdle in application because regions immediately adjacent to the needle are certainly ablated; confirming the location of the outer boundary of the ablation is more crucial. Results in a recent paper by Deffieux *et al.* [56] suggest that the uncertainty in measuring higher shear wave velocities is inherently higher. This indicates there is a lower limit to how accurately SWV maps can be reconstructed inside the stiff inclusion.

A visible side effect of the sheaf imaging strategy is the “wheel spoke” artifact seen in Fig. 8, especially when using fewer planes in the sheaf. These appear as radial streaks emanating from the center of the C-plane and coinciding with the radial locations of the image planes over which ultrasound echo data was acquired. The smoothing parameter can be manually tuned to get rid of such artifacts—a larger value of  $\eta$  will smooth out such variations. In a commercial system, there may be regulatory hurdles to allowing the user to control the value of  $\eta$ , but it may be possible to include an additional preset akin to smoothing and edge enhancement which is available on almost all ultrasound scanners.

The phantom experiment setup in this paper was designed to mimic a liver ablation procedure. In other real world situations, it may be more challenging to align the needle along the axial beam direction of the

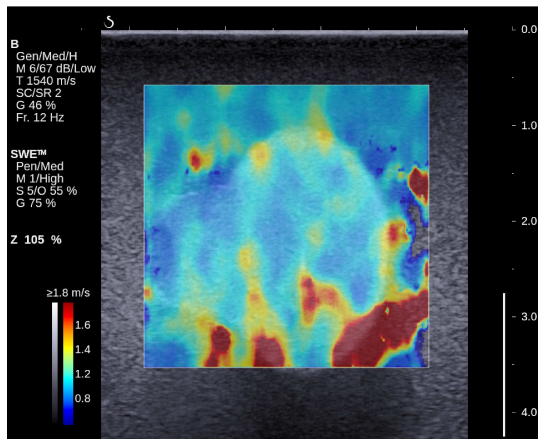


Fig. 12. A “bronze standard” SWV image of the phantom inclusion corresponding to the same imaging plane of Fig. 7(a). This image was acquired using a Supersonic Imagine ultrasound scanner with the shear wave imaging mode. (Original image has been cropped and rearranged to fit.)

transducer. In situations where the needle is at an angle to the axial ultrasound beam direction, 2D displacement tracking algorithm can be used. The component of these displacements parallel to the needle can be extracted and TTP values along lines perpendicular to the needle can be calculated in steps 2 and 3 of Section II-C, respectively. In case of physical constraints on placing the transducer around the needle, it may be impossible to obtain the complete sheaf, resulting in voids in the dataset. But a partial volume reconstruction can still be obtained using the same algorithm presented in this paper, using only that part of the fine grid where data points are present. The four step decomposition offers good flexibility for tuning the details of each signal processing block for specific applications. For example, some commercial ultrasound scanners already offer imaging modes to map shear wave velocities (either as point estimates or over large regions) irrespective of the alignment of the image plane with respect to the needle. In such systems, it will be convenient to incorporate one additional block for step 4 at the end of the existing signal processing chain to generate 3D volume maps.

It is also useful to compare the SWV image plane reconstruction with a “bronze standard” image acquired from a commercial Supersonic Imagine ultrasound scanner with shear wave imaging capability. Fig. 12 shows one image plane of the phantom with a SWV overlay on B-mode. The image plane is identical to the one shown in Figs. 7(a) and (b). Note that high velocity artifacts can be seen at depths greater than 2.5 cm.

Results in this paper indicate that 6 planes in a sheaf are sufficient for fast reconstruction in the particular TM phantom used, both qualitatively and quantitatively.

This is because the shape of the inclusion was mostly symmetric about the needle, (except for a small irregularly shaped partially ablated region). This was also confirmed by the simulation experiment that was specifically used to mimic the situation in the phantom experiment. Greater number of image planes may be needed if the inclusion is more irregularly shaped. More complex geometries can be simulated ahead of time using the method described in Section II-C4 to decide on a suitable number of image planes in the sheaf as part of pre-ablation clinical planning.

The location and number of angular planes can also be optimized with the aim of minimizing the number of planes required for effective 3D reconstruction while maximizing the processing speed. This will also allow implementation of 3D reconstruction algorithms on low end commercial ultrasound systems which may not be equipped with sufficient processing power or modern graphical processing units (GPUs). Minimization of the number of planes will enable faster data acquisition and processing for eventual real-time implementation of 3D SWV volume reconstructions. Adaptive or non-uniform sampling of complex regions, for example those including the simulated, partially ablated regions as shown in Figs. 7–8 and regions near large vessels during *in vivo* implementations, will have to be evaluated to determine if this can further improve delineation. Data can be acquired in multiple passes where the interpolated visualization from an earlier pass provides feedback for sampling critical locations in the volume, enabling an adaptive sampling approach for improved delineation.

Although the sheaf pattern of acquisition is naturally suited to the geometry of the EVE setup, an inherent limitation of this method is that every image plane must contain the needle to enable time of arrival estimation. In a sheaf, data samples progressively get sparser away from the needle. This shortcoming can be addressed by sampling extra planes in the sheaf so that a certain fine sample spacing is achieved at a predetermined distance away from the needle. Alternatively, if a specific ROI has already been located, imaging planes that are not uniformly spaced in angle can be employed; finer spacing in specific regions may provide better reconstruction quality at those locations. Knowledge from earlier iterations of the reconstruction algorithm may also be incorporated in the interpolation procedure, by reconstructing only parts of the full volume that are known to contain any interesting features, either automatically or with the intervention of a clinician.

## V. CONCLUSION

Monitoring tumor ablations to determine the spatial extent of treatment is fundamentally a 3D problem. 3D imaging is essential to determine if the entire tumor and surrounding margins have been successfully ablated to ensure favorable outcomes from this minimally invasive procedure. Current 3D ultrasound imaging using wobbler transducers are inefficient in depicting ablation volumes as imaging planes are collected in a raster fashion. By exploiting the axis of symmetry about the ablation needle, the SOUPR algorithm developed in this paper provides good 3D visualization using significantly fewer planes and faster 3D reconstructions. Various image quality statistics evaluated using independent datasets indicate that the SOUPR algorithm provides good contrast between the tumor and surrounding softer regions. Moreover, the algorithms presented in this paper can be easily extended to process other types of data (such as strain) to produce similar C-plane reconstructions for visualization of ablated regions.

## REFERENCES

- [1] J. Ferlay, H. Shin, F. Bray, D. Forman, C. Mathers, and D. Parkin, "Globocan 2008 v2.0, cancer incidence and mortality worldwide: Iarc cancerbase no. 10 [internet]," Lyon, France, 2010, available from: <http://globocan.iarc.fr>, accessed on Sep. 11, 2013.
- [2] K. E. Maturen, A. P. Wasnik, J. E. Bailey, E. G. Higgins, and J. M. Rubin, "Posterior acoustic enhancement in hepatocellular carcinoma," *J. Ultrasound Med.*, vol. 30, no. 4, pp. 495–499, Apr. 2011.
- [3] C. Cha, J. F. T. Lee, J. Gurney, B. Markhardt, T. Warner, F. Kelcz, and D. Mahvi, "CT versus sonography for monitoring radiofrequency ablation in a porcine liver," *Am. J. Roentgenol.*, vol. 175, no. 3, pp. 705–711, Sep. 2000.
- [4] M. G. van Vledder, M. S. Torbenson, T. M. Pawlik, E. M. Boctor, U. M. Hamper, K. Olino, and M. A. Choti, "The effect of steatosis on echogenicity of colorectal liver metastases on intraoperative ultrasonography," *Arch. Surg.*, vol. 145, no. 7, pp. 661–667, Jul. 2010.
- [5] L. Gao, K. Parker, R. Lerner, and S. Levinson, "Imaging of the elastic properties of tissue—A review," *Ultrasound Med. Biol.*, vol. 22, no. 8, pp. 959–977, May 1996.
- [6] T. Varghese, J. Zagzebski, and F. L. Jr., "Elastographic imaging of thermal lesions in the liver in vivo following radiofrequency ablation: preliminary results," *Ultrasound Med. Biol.*, vol. 28, no. 11–12, pp. 1467–1473, Nov.-Dec. 2002.
- [7] S. Bharat and T. Varghese, "Radiofrequency electrode vibration-induced shear wave imaging for tissue modulus estimation: A simulation study," *J. Acoust. Soc. Am.*, vol. 128, no. 4, pp. 1582–1585, Oct. 2010.
- [8] R. DeWall, T. Varghese, and E. Madsen, "Shear wave velocity imaging using transient electrode perturbation: Phantom and ex vivo validation," *IEEE Trans. Med. Imag.*, vol. 30, no. 3, pp. 666–678, Mar. 2011.
- [9] A. H. Henni, C. Schmitt, and G. Cloutier, "Three-dimensional transient and harmonic shear-wave scattering by a soft cylinder for dynamic vascular elastography," *J. Acoust. Soc. Am.*, vol. 124, no. 4, pp. 2394–2405, Oct. 2008.
- [10] J. McLaughlin and D. Renzi, "Shear wave speed recovery in transient elastography and supersonic imaging using propagating fronts," *Inv. Prob.*, vol. 22, no. 2, pp. 681–706, Mar. 2006.
- [11] O. Kolokythas, T. Gauthier, A. T. Fernandez, H. Xie, B. A. Timm, C. Cuevas, M. K. Dighe, L. M. Mitsumori, M. F. Bruce, D. A. Herzka, G. K. Goswami, R. T. Andrews, K. M. Oas, T. J. Dubinsky, and B. H. Warren, "Ultrasound-based elastography: a novel approach to assess radio frequency ablation of liver masses performed with expandable ablation probes: A feasibility study," *J. Ultrasound Med.*, vol. 27, no. 6, pp. 935–946, Jun. 2008.
- [12] N. Rubert, S. Bharat, R. J. DeWall, A. Andreano, C. Brace, J. Jiang, L. Sampson, and T. Varghese, "Electrode displacement strain imaging of thermally-ablated liver tissue in an in vivo animal model," *Med. Phys.*, vol. 37, no. 3, pp. 1075–1082, Mar. 2010.
- [13] J. Jiang, C. Brace, A. Andreano, R. J. DeWall, N. Rubert, T. G. Fisher, T. Varghese, F. Lee, and T. J. Hall, "Ultrasound-based relative elastic modulus imaging for visualizing thermal ablation zones in a porcine model," *Phys. Med. Biol.*, vol. 55, no. 8, pp. 2281–2306, Apr. 2010.
- [14] H. J. Kwon, M. J. Kang, J. H. Cho, J. Y. Oh, K. J. Nam, S. Y. Han, and S. W. Lee, "Acoustic radiation force impulse elastography for hepatocellular carcinoma-associated radiofrequency ablation," *World J. Gastroenterol.*, vol. 17, no. 14, pp. 1874–1878, Apr. 2011.
- [15] T. Varghese, "Quasi-Static Ultrasound Elastography," *Ultrasound Clin.*, vol. 4, no. 3, pp. 323–338, Jul. 2009.
- [16] E. Boctor, M. Choti, R. Ghanem, R. Taylor, G. Hager, G. Fichtinger *et al.*, "Ultrasound monitoring of tissue ablation via deformation model and shape priors," in *Medical Image Computing and Computer-Assisted Intervention—MICCAI 2006*. Springer Berlin Heidelberg, 2006, pp. 405–412.
- [17] B. Fahey, S. Hsu, P. Wolf, R. Nelson, and G. Trahey, "Liver ablation guidance with acoustic radiation force impulse imaging: challenges and opportunities," *Phys. Med. Biol.*, vol. 51, no. 15, pp. 3785–3808, Jul. 2006.
- [18] M. H. Wang, M. L. Palmeri, C. D. Guy, L. Yang, L. W. Hedlund, A. M. Diehl, and K. R. Nightingale, "In vivo quantification of liver stiffness in a rat model of hepatic fibrosis with acoustic radiation force," *Ultrasound Med. Biol.*, vol. 35, no. 10, pp. 1709–1721, Oct. 2009.
- [19] M. Muller, J.-L. Gennisson, T. Defieux, M. Tanter, and M. Fink, "Quantitative viscoelasticity mapping of human liver using supersonic shear imaging: Preliminary in vivo feasibility study," *Ultrasound Med. Biol.*, vol. 35, no. 2, pp. 219–229, Feb. 2009.
- [20] L. Sandrin, M. Tanter, S. Catheline, and M. Fink, "Shear modulus imaging with 2-D transient elastography," *Ultrasonics*, vol. 49, no. 4, pp. 426–435, Dec. 2002.
- [21] M. Orescanin, M. Qayyum, K. Toohey, and M. Insana, "Dispersion and shear modulus measurements of porcine liver," *Ultrason. Imag.*, vol. 32, no. 4, pp. 255–266, Oct. 2010.
- [22] S. T. Elliott, "Volume ultrasound: the next big thing?" *Br. J. Radiol.*, vol. 81, no. 961, pp. 8–9, Jan. 2008.
- [23] H. Cardinal, J. Gill, and A. Fenster, "Analysis of geometrical distortion and statistical variance in length, area, and volume in a linearly scanned 3-D ultrasound image," *IEEE Trans. Med. Imag.*, vol. 19, no. 6, pp. 632–651, Jun. 2000.
- [24] R. S. José-Estépar, M. Martín-Fernández, P. Caballero-Martínez, C. Alberola-López, and J. Ruiz-Alzola, "A theoretical framework to three-dimensional ultrasound reconstruction from irregularly sampled data," *Ultrasound Med. Biol.*, vol. 29, no. 2, pp. 255–269, Feb. 2003.
- [25] J. E. Lindop, G. M. Treece, A. H. Gee, and R. W. Prager,

- “3D elastography using freehand ultrasound,” *Ultrasound Med. Biol.*, vol. 32, no. 4, pp. 529–545, Apr. 2006.
- [26] H. Rivaz, I. Fleming, L. Assumpcao, G. Fichtinger, U. Hamper, M. Choti, G. Hager, and E. Boctor, “Ablation monitoring with elastography: 2D in-vivo and 3D ex-vivo studies,” in *Medical Image Computing & Computer-Assisted Intervention—MICCAI 2008*, vol. 11, no. 2, 2008, pp. 458–466.
- [27] M.-A. Janvier, G. Soulez, L. Allard, and G. Cloutier, “Validation of 3D reconstructions of a mimicked femoral artery with an ultrasound imaging robotic system,” *Med. Phys.*, vol. 37, no. 7, pp. 3868–3879, Jun. 2010.
- [28] S. Bharat, T. G. Fisher, T. Varghese, T. J. Hall, J. Jiang, E. L. Madsen, J. A. Zagzebski, and F. T. Lee Jr, “Three-dimensional electrode displacement elastography using the Siemens C7F2 fourSight four-dimensional ultrasound transducer,” *Ultrasound Med. Biol.*, vol. 34, no. 8, pp. 1307–1316, Aug. 2008.
- [29] P. Foroughi, G. Hager, and E. Boctor, “Robust elasticity imaging using external tracker,” in *IEEE International Symposium on Biomedical Imaging: From Nano to Macro, 2009 (ISBI 2009)*, Jun. 2009, pp. 209–212.
- [30] A. V. Patil, C. D. Garson, and J. A. Hossack, “3D prostate elastography: algorithm, simulations and experiments,” *Phys. Med. Biol.*, vol. 52, no. 12, pp. 3643–3663, Jun. 2007.
- [31] L. Zhai, J. Madden, W. C. Foo, V. Mouraviev, T. J. Polascik, M. L. Palmeri, and K. R. Nightingale, “Characterizing stiffness of human prostates using acoustic radiation force,” *Ultrason. Imag.*, vol. 32, no. 4, pp. 201–213, Oct. 2010.
- [32] S. H. Lee, J. M. Chang, W. H. Kim, M. S. Bae, N. Cho, A. Yi, H. R. Koo, S. J. Kim, J. Y. Kim, and W. K. Moon, “Differentiation of benign from malignant solid breast masses: comparison of two-dimensional and three-dimensional shear-wave elastography,” *Eur. Radiol.*, vol. 23, no. 4, pp. 1015–1026, Apr. 2013.
- [33] M. Wang, B. Byram, M. Palmeri, N. Rouze, and K. Nightingale, “Imaging transverse isotropic properties of muscle by monitoring acoustic radiation force induced shear waves using a 2-D matrix ultrasound array,” *IEEE Trans. Med. Imag.*, vol. 32, no. 9, pp. 1671–1684, Sep. 2013.
- [34] R. Sinkus, J. Lorenzen, D. Schrader, M. Lorenzen, M. Dargatz, and D. Holz, “High-resolution tensor MR elastography for breast tumour detection,” *Phys. Med. Biol.*, vol. 45, no. 6, pp. 1649–1664, Jun. 2000.
- [35] M. Tanter, M. Pernot, G. Montaldo, J.-L. Gennisson, E. Bavu, E. Mace, T.-M. Nguyen, M. Couade, and M. Fink, “Real time quantitative elastography using supersonic shear wave imaging,” in *Proc. 2010 IEEE Intl. Symp. on Biomed. Imag.: From Nano to Macro*, Apr. 2010, pp. 276–279.
- [36] A. Baghani, A. Brant, S. Salcudean, and R. Rohling, “A high-frame-rate ultrasound system for the study of tissue motions,” *IEEE Trans. Ultrason., Ferroelectr., Freq. Control*, vol. 57, no. 7, pp. 1535–1547, Jul. 2010.
- [37] P. Abolmaesumi, S. Salcudean, W.-H. Zhu, M. Sirouspour, and S. DiMaio, “Image-guided control of a robot for medical ultrasound,” *IEEE Trans. Robot. Autom.*, vol. 18, no. 1, pp. 11–23, Feb. 2002.
- [38] E. Madsen, G. Frank, M. Hobson, H. Shi, J. Jiang, T. Varghese, and T. Hall, “Spherical lesion phantoms for testing the performance of elastography systems,” *Physics in Medicine and Biology*, vol. 50, no. 24, pp. 5983–5995, Dec. 2005.
- [39] M. L. Palmeri, M. H. Wang, J. J. Dahl, K. D. Frinkley, and K. R. Nightingale, “Quantifying hepatic shear modulus in vivo using acoustic radiation force,” *Ultrasound Med. Biol.*, vol. 34, no. 4, pp. 546–558, Apr. 2008.
- [40] T. Varghese and J. Ophir, “A theoretical framework for performance characterization of elastography: the strain filter,” *IEEE Trans. Ultrason., Ferroelectr., Freq. Control*, vol. 44, no. 1, pp. 164–172, Jan. 1997.
- [41] M. Elkateb Hachemi, S. Calle, and J. P. Remenieras, “Transient displacement induced in shear wave elastography: comparison between analytical results and ultrasound measurements,” *Ultrasonics*, vol. 44 Suppl 1, pp. e221–225, Dec. 2006.
- [42] K. Nightingale, D. Stutz, R. Bentley, and G. Trahey, “Acoustic radiation force impulse imaging: ex vivo and in vivo demonstration of transient shear wave propagation,” in *Proc. 2002 IEEE Intl. Symp. on Biomed. Imag., 2002*, Jun. 2002, pp. 525–528.
- [43] A. Ingle and T. Varghese, “A comparison of model based and direct optimization based filtering algorithms for shearwave velocity reconstruction for electrode vibration elastography,” in *IEEE 10th International Symposium on Biomedical Imaging (ISBI 2013)*, 2013, pp. 760–763.
- [44] J. Nocedal and S. J. Wright, *Numerical Optimization*, 2nd ed. New York: Springer, 2006.
- [45] S. Kirkpatrick, C. D. Gelatt, and M. P. Vecchi, “Optimization by simulated annealing,” *Science*, vol. 220, no. 4598, pp. 671–680, May 1983.
- [46] H. Akaike, “A new look at the statistical model identification,” *IEEE Trans. Autom. Control*, vol. 19, no. 6, pp. 716–723, Dec. 1974.
- [47] G. Wahba, *Spline Models for Observational Data*, ser. CBMS-NSF Regional Conference Series in Applied Mathematics. Society for Industrial and Applied Mathematics, 1990.
- [48] L. Wasserman, *All of Nonparametric Statistics (Springer Texts in Statistics)*. Springer, Oct. 2005.
- [49] T. Varghese and J. Ophir, “An analysis of elastographic contrast to noise ratio,” *Ultrasound Med. Biol.*, vol. 24, no. 6, pp. 915–924, Jul. 1998.
- [50] G. James, D. Witten, T. Hastie, and R. Tibshirani, *An Introduction to Statistical Learning: with Applications in R*, ser. Springer Texts in Statistics. Springer, 2013.
- [51] M. H. Wang, M. L. Palmeri, V. M. Rotemberg, N. C. Rouze, and K. R. Nightingale, “Improving the robustness of time-of-flight based shear wave speed reconstruction methods using RANSAC in human liver in vivo,” *Ultrasound Med. Biol.*, vol. 36, no. 5, pp. 802–813, May 2010.
- [52] H. Rivaz, E. M. Boctor, M. A. Choti, and G. D. Hager, “Real-time regularized ultrasound elastography,” *IEEE Trans. Med. Imag.*, vol. 30, no. 4, pp. 928–945, Apr. 2011.
- [53] H. Rivaz, E. Boctor, P. Foroughi, R. Zellars, G. Fichtinger, and G. Hager, “Ultrasound elastography: A dynamic programming approach,” *IEEE Trans. Med. Imag.*, vol. 27, no. 10, pp. 1373–1377, Oct. 2008.
- [54] R. J. DeWall and T. Varghese, “Improving thermal ablation delineation with electrode vibration elastography using a bidirectional wave propagation assumption,” *IEEE Trans. Ultrason., Ferroelectr., Freq. Control*, vol. 59, no. 1, pp. 168–173, Jan. 2012.
- [55] J. Klein, J. McLaughlin, and D. Renzi, “Improving arrival time identification in transient elastography,” *Phys. Med. Biol.*, vol. 57, no. 8, pp. 2151–2168, Apr. 2012.
- [56] T. Defieux, J.-L. Gennisson, B. Larrat, M. Fink, and M. Tanter, “The variance of quantitative estimates in shear wave elastography: Theory and experiments,” *IEEE Trans. Ultrason., Ferroelectr., Freq. Control*, vol. 59, no. 11, pp. 2390–2410, Nov. 2012.